

Contents lists available at ScienceDirect

## International Journal of Plasticity

journal homepage: http://www.elsevier.com/locate/ijplas



# Quantifying the dynamics of dislocation kinks in iron and tungsten through atomistic simulations



Rigelesaiyin Ji <sup>a</sup>, Thanh Phan <sup>a</sup>, Hao Chen <sup>b</sup>, Liming Xiong <sup>a,\*</sup>

- <sup>a</sup> Department of Aerospace Engineering, Iowa State University, Ames, IA, 50011, USA
- b Key Laboratory of Pressure Systems and Safety, Ministry of Education, School of Mechanical and Power Engineering, East China University of Science and Technology, Shanghai, 200237, People's Republic of China

#### ARTICLE INFO

Keywords:
Dislocation
Kink dynamics
Atomistic simulations
Local stress
Multiscale modeling

#### ABSTRACT

When high-Peierls-barrier materials such as iron (Fe) and tungsten (W) are deformed, dislocation kinks can be easily activated. The subsequent kink dynamics may dictate the dislocation mobility and the material's overall performance under certain conditions. In this work, taking the thermalinduced kink diffusion along ½<111> screw dislocation lines as an example, the kink dynamics in b.c.c. iron and tungsten are quantified through atomistic simulations. Results show that in both Fe and W, the kink dynamics, including its diffusion coefficient (Dkink) and dissipation parameter  $(\gamma_{kink})$ , are sensitive to the dimension (noted as L) of a simulation cell size along the dislocation line direction: the larger L, the higher  $D_{kink}$ , and the smaller  $\gamma_{kink}$ . A scaling law for describing the three-stage L-dependent kink dynamics is extracted from a series of computational analysis of the kink diffusion along dislocations with L ranging from tens to hundreds of nanometers. It is found that, if a converged  $D_{kink}$  is desired from atomistic simulations, the minimum L needs to be at least hundreds of nanometers. This is beyond the reach of an atomic-level model using a modest computational resource. To explain the L-dependent kink dynamics, we calculate the kinkinduced local stress fields using two different atomistic stress formula, i.e., a widely-used Virial and a recently developed mechanical stress formula. Results suggest: (i) the L-dependent kink dynamics is caused by the long-range elastic interaction between the kink and its periodic images; and (ii) the Virial stress formula underestimates such interactions. This work lays the continuum description of kink-controlled dislocation dynamics on an atomistic foundation. It will also support the development of multiscale methods for addressing the coupled dynamics between the motion of a µm-long dislocation line and the atomic-level kink diffusion along the line itself in b.c. c. metals or other high-Peierls-barrier materials under deformation.

#### 1. Introduction

Dislocations are considered as major carriers of plasticity in many materials, and their mobility in turn determines the material's plastic deformation rate at the macroscopic level. Therefore, extensive research has been devoted to formulating dislocation mobility laws (Cai and Bulatov, 2004; Groh et al., 2009; Po et al., 2016; Kooiman et al., 2015; Gurrutxaga-Lerma, 2016; Proville and Rodney, 2018), which relate an applied stress with dislocation velocities by considering the balance between the force acting on a dislocation core and the lattice friction. Due to the planner dislocation core structure and low lattice resistance, the plastic flow in f.c.c. metals is

E-mail address: lmxiong@iastate.edu (L. Xiong).

<sup>\*</sup> Corresponding author.

mainly mediated by dislocation gliding. Correspondingly, the formulation and calibration of a dislocation mobility law in such materials is always a simplest practice to start with and is considered to be well developed (Cai and Bulatov, 2004). Distinct from f.c.c. solids, the b.c.c. material or h.c.p. crystals, such as Mg, usually presents a high Peierls barrier, and the dislocation motion in them can be largely controlled by the activities of kinks (sudden deviations from a straight dislocation line on atomic dimensions), especially when the stress level and environment temperature is not high (Lothe and Hirth, 1959). For instance, a recent experiment by Srivastava and his co-workers showed that the kink migration is a dominant mechanisms responsible for the screw dislocation gliding on the <c+a> pyramidal slip plane in h.c.p. Mg crystals (Srivastava and El-Awady, 2017). In this scenario, the interplay between dislocation line migrations and the kink diffusion along the line itself induces an extreme complexity. It necessitates a fundamental understanding on how the kink dynamics controls the dislocation behavior, in particular, when predicting the mechanical performance of b.c.c. or h.c. p. metals under plastic deformation becomes an aim.

In the past several decades, a large amount of theoretical (Lothe and Hirth, 1959; Brailsford, 1965; Eshelby, 1962; Seeger and Holzwarth, 2006; Duesbery, 1983; Rodney and Proville, 2009; Pi et al., 2017) and computational (Weinberger et al., 2013; Proville et al., 2013; Swinburne et al., 2013; Dezerald et al., 2015; Lim et al., 2015) research has been conducted to connect kink dynamics with dislocation motions in b.c.c. metals. For example, in a pioneering work by Lothe and Hirth (1959), the dislocation velocity (v) was related with kink diffusion through  $v_D = \frac{D_{kink}}{E_n T} F$ , in which  $D_{kink}$  is the kink diffusion coefficient,  $k_B$  is the Boltzmann constant, T is the temperature, and F is a thermodynamic force. Such dislocation mobility laws can be very useful in higher-length-scale computer models, such as dislocation dynamics (DD) (Van der Giessen and Needleman, 1995; Zbib et al., 2000; Ghoniem et al., 2000; Bulatov et al., 2006; Wang and Beyerlein, 2011; Huang and Li, 2013; Srivastava et al. 2013; Li et al., 2014; Hussein et al., 2015; El-Awady, 2015), phase field (PF) (Koslowski et al., 2002; Levitas and Javanbakht, 2014), kinetic Monte Carlo (kMC) (Lin and Chrzan, 1999; Cai et al., 2001; Shinzato et al., 2019), crystal plasticity (Weinberger et al., 2012; Patra et al., 2014; Amodeo et al., 2016; Patra and McDowell, 2016; Tallman et al., 2017), or some other multiscale models (Kuchnicki et al., 2008; Swinburne et al., 2013). For instance, through considering the kink motion as a combination of thermal-induced diffusion and local stress-driven drift, using kink nucleation energy and kink mobility as inputs, the kMC models describe the dislocation motion as a consequence of kink activation, migration, and recombination. By treating the kinks on long (~27 µm in length) dislocation lines as short (2.5 Å in height) pure edge segments, such kMC models indeed offer a strategy for bridging two extreme length scales, although in an approximated manner. By contrast, in DD models, the thermally-assisted kink nucleation and subsequent lateral kink migration in b.c.c. metals are implicitly incorporated into the mobility laws (Naamane et al., 2010; Tang and Marian, 2014). Although the atomic-scale kinks are not explicitly tracked, equipped with the phenomenological mobility laws, a DD model does provide a mesoscopic description of dislocation dynamics in b.c. c. metals (Po et al., 2016). Clearly, both kMC and DD are applicable to characterize the dynamics of long dislocations in b.c.c. metals, but both of them require the mobility laws to be calibrated upon a clear-cut understanding of the kink dynamics at the atomic level. This is especially true when b.c.c. metals are subjected to a low stress at finite temperatures. In this situation, the kink dynamics controls the behavior of dislocations and needs to be understood from the bottom up.

Fortunately, with the advent of high-performance computing, the atomistic model, such as molecular dynamics (MD), has evolved as a powerful tool for understanding the kink dynamics due to its capability in retaining the angstrom-level core structures of material defects. For example, recent atomistic simulation (Swinburne et al., 2013; Stukowski et al., 2015) of b.c.c. materials containing isolated kinks shows that, not surprisingly, the higher the temperature, the faster the kink diffuse along a dislocation line. Such results can be used to develop the temperature-dependent dislocation mobility laws for kMC and DD (Gilbert et al., 2011; Cereceda et al., 2013). Nevertheless, at the current stage, due to the length scale limitations (tens of nanometers and even below in terms of a dislocation line length) of MD models, great care needs to be taken when directly informing these atomistic simulation results into kMC and DD, both of which are mesoscopic models and actually need the mobility laws for very long dislocations lines as the inputs. In order to achieve a reasonable accuracy, the mobility laws for kMC or DD should be always mechanism-based and need to retain the real physics of kink dynamics as much as possible. This necessitates the kink diffusion along the long (micrometer or above) dislocation lines to be correctly extrapolated, if it cannot be directly characterized, from the atomistic models. Otherwise, it will be challenging for a kMC or DD to produce the physically reasonable kink-controlled dislocation dynamics, such as a line length-dependent dislocation mobility (Caillard, 2010, 2013), in b.c.c. materials.

Aiming to quantify the dislocation line length-dependent kink dynamics, we perform a series of atomic-level computational analysis of kink diffusion along dislocation lines in iron and tungsten. This paper is organized as follows: in section II, we briefly introduce the chosen materials and the computational set-up including the boundary conditions, the interatomic potential, as well as the strategy of building the isolated dislocation kinks in an atomistic model. Simulation results are analyzed in Section III. It contains: (i) a tracking of the motion of a single kink and a calculation of the kink's mean square displacement, from which the kink diffusion coefficients ( $D_{kink}$ ) and dissipation parameter ( $\gamma_{kink}$ ) are extracted; (ii) a calibration of the scaling laws that can be used for describing the L-dependent kink diffusion in Fe and W; and (iii) an atomic-level measurement of the kink-kink interaction through the analysis of kink-induced stress fields using a Virial as well as a recently developed mechanical stress formula (Chen, 2016; Chen and Diaz, 2016, 2018). The atomistic data is also compared with the classical elasticity solutions. This may provide an explanation on why the kink dynamics is sensitive to the length of a dislocation line along which it diffuses. Section IV summarizes our major findings, the potential applications of the obtained results together with a discussion of the future research along this direction.

#### 2. Computational set-up

Two typical b.c.c. metals, Fe and W, are chosen as the model materials here because: (a) Fe and W are widely used in engineering

infrastructures where the dislocation-mediated plastic deformation is one major concern; (b) studies of the dislocation kink dynamics in these two materials are representative because Fe and W fall into two extreme categories: Fe is highly anisotropic and W is considered to be nearly isotropic instead (Anderson et al., 2017); and (c) in addition to many experimental studies (Caillard, 2010, 2013; El-Atwani et al., 2014; Terentyev et al., 2014; Kim et al., 2010), extensive MD simulations of dislocations in Fe and W using a variety of different interatomic force fields have been reported (Verschueren et al., 2018; Xu et al., 2017a; Wen and Ngan, 2000; Gordon et al., 2010). This provides not only a variety of reliable interatomic potentials but also a large amount of data for cross-validation. Here the Mendelev interatomic potential (Gordon et al., 2011) derived from the embedded atom method (EAM) is used for Fe, and an EAM force field developed by Marinica et al. (2013) is used for W. These two potentials have been successfully demonstrated in: (i) describing the non-degenerate core structures and properties of screw dislocations (Domain and Monnet, 2005; Ventelon and Willaime, 2007; Frederiksen and Jacobsen, 2003; Chaussidon et al., 2006; (ii) characterizing kink structure and formation energies (Gordon et al., 2010; Ventelon et al., 2009; Chaussidon et al., 2006; Rodney and Proville, 2009); and (iii) capturing the temperature-dependent kink diffusion in Fe and W (Swinburne et al., 2013; Stukowski et al., 2015).

In order to characterize the dynamics of kink diffusion along a dislocation line in Fe and W by MD, as a first step, the atomistic computer models containing kinked dislocations are constructed (Fig. 1a). In Fig. 1a, the sample is visualized using OVITO (Stukowski, 2009). Here only the dislocated (blue) and the surface atoms (gray) are displayed. A series of atomistic models (seven for Fe and six for W) with their dimensions along the dislocation line direction (y direction in Fig. 1a) spanning from 30 nm to 450 nm are built. The dimension of the simulation cell along z direction is 15 nm. Then the resulting total number of atoms is from 2.5 to 37 million for Fe, and is from 1.6 to 22 million for W. The periodic boundary conditions (PBCs) are applied along the x and y directions while z direction is set to be free. It should be mentioned that the b.c.c. sample with a single built-in screw dislocation will have a net Burgers vector. This will lead to a divergent elastic energy. To avoid such a scenario, we build a dislocation dipole (Fig. 1a) into the model according to the displacement field solution from the theory of elasticity. The initial separation between the two dislocations in the dipole is set to be 40 nm (Fig. 1b). Due to the opposite Burgers vectors in a dipole set-up, the two dislocation lines will attract each other. Such an attractive force may drive dislocations to move. If that happens, it will lead to coupled dynamics between dislocation motion and kink diffusion along the dislocation lines, which is, of course, very important but not the focus of this work at this stage. In order to balance out the attractive force between those two dislocations in the dipole, the dimension of the simulation cell along x direction has to be sufficiently large such that this attractive force can be perfectly canceled by the interaction between each dislocation and its nearest periodic images (Fig. 1b). Under this consideration, in all the atomistic models for Fe and W, the dimension of the simulation cell along the x direction is set to be 80 nm (Fig. 1b).

Thereafter, instead of modeling the kink nucleation process, the isolated kinks are intially introduced on each of the dislocation lines in the dipole. It should be noted that, because the b.c.c. crystal structure is not mirror symmetric along the <111> direction, there exist two types of dislocation kinks, i.e., 'left' and 'right' kinks (Bulatov et al., 1997; Marinica et al., 2013; Stukowski et al., 2015). Here we focus on quantifying the dynamics of the 'right' kink. There is one technical difficulty when introducing a single kink on a dislocation line in the atomistic model because the kink vector is not aligned with any periodic vector of the crystal. To overcome this difficulty, following the approach by Ventelon et al. (2009), we build the 'right' kink with a vector of ½ [111] in the two dislocation lines through imposing a tilt, 1/3[121]-1/6[111], on the simulation cell along the y direction. Such a tilt component was deduced from elasticity calculations for perfect dislocations in a quadrupolar arrangement (Ventelon and Willaime, 2007; Li et al., 2004). It can reserve the periodicity along the dislocation line direction (y direction in Fig. 2a). To elucidate this tilting procedure, Fig. 2a shows the projection of a tilted simulation cell (solid lines) on the xy plane and its comparison with an un-tilted cell (dash lines). Under this tilting, kinks will occur (noted as Kink-I and Kink-II in Fig. 2a). This approach yields the same type of kink (the 'right' kink here) on both dislocation lines. They appear as localized geometric and energetic regions, which deviate from the core configuration and energy of an originally straight dislocation line. In Fig. 2a, through displaying the dislocation core atoms in blue and the higher-energy atoms in progressively red, the initial position of the two kinks can be located. As a demonstration of the kink core structure, the atoms nearest to the geometric center of a kinked dislocation are also shown in Fig. 2b. Those atoms are connected by arrows indicating relative atomic displacements along the dislocation line in a helical sequence (Fig. 2b). It is seen that, different from the 'left' kink with two extra atoms in a helical sequence along the core of a screw dislocation (Bulatov et al., 1997), the 'right' kink appears with only one extra atom (the red atom in Fig. 2b).

After introducing kinks into the model, the atomistic systems are equilibrated at zero temperature in LAMMPS (Plimpton, 1995) using a conjugated gradient algorithm. The initially introduced kinks are sharp before the equilibration but become smooth thereafter.

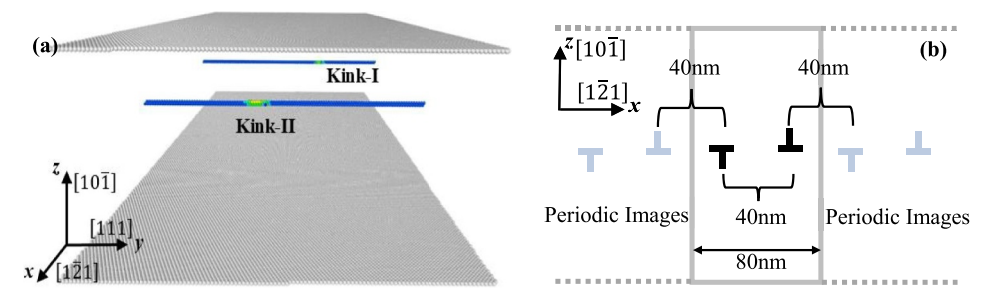
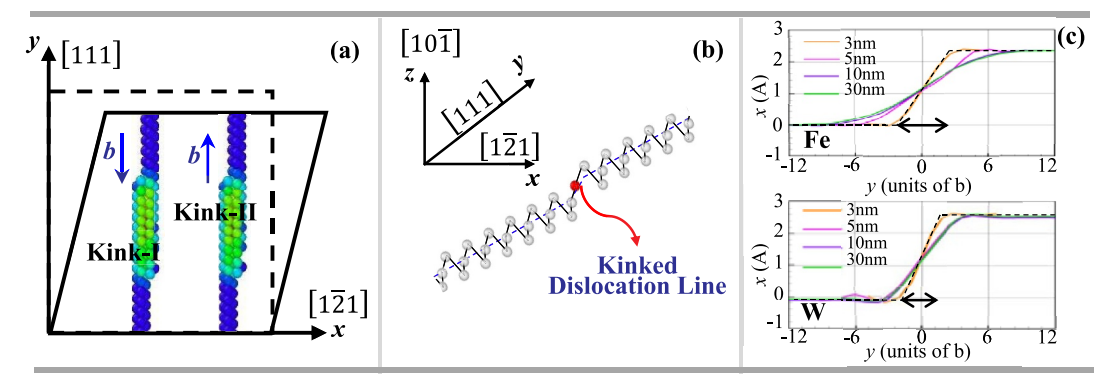


Fig. 1. Atomistic model containing a dislocation dipole: (a) kinked dislocation lines; (b) dimensions.



**Fig. 2.** Atomistic models of dislocation kinks: (a) building a kink on each dislocation line through tilting the simulation cell in *xy* plane; (b) the core structure of a kinked dislocation before relaxation; (c) the shape of a 'right' kink after relaxation and its dependence on *L* in Fe and W.

Fig. 2c shows the shape of a kink along different dislocation lines with their lengths spanning from 3 nm to 30 nm. Here the configurations of the dislocation lines are extracted through connecting the centers of the gravity of the dislocation core atoms in each (111) plane along the y direction. The kink-induced deviation, noted as h, from the center of the dislocation line along the z direction is normalized by the distance between two nearest Peierls valleys  $\sqrt{6}a/3$ , where a is the lattice constant of b.c.c. crystals. Based on the dislocation line configuration in Fig. 2c, the equilibrium kink width, w, can be measured as the distance over which z (y) varies from 0.05h to 0.95h. Fig. 2c shows that, in iron, w is  $\sim$ 2 nm for the kink on a 3 nm-long dislocation line, and remains to be  $\sim$ 6 nm on dislocation lines with their lengths changing from 10 nm to 30 nm. Similarly, in tungsten, w is  $\sim$ 1 nm when L is 3 nm and remains as  $\sim$ 2.3 nm when L changes from 10 nm to 30 nm. Clearly, in both Fe and W, the kink width strongly depends on L when L is very small but converges when L is sufficiently large (30 nm and above). Such an L-dependent kink width is believed to be caused by the repulsive interaction between the kink and its periodic images, which will be discussed and analyzed in a later section of this paper. Also, in order to support the development of the higher length scale computer models for describing dislocation kinks, here the shape of the equilibrated kinks along the dislocations in Fig. 2c is fitted to a commonly-used functional form in kMC models (Stukowski et al., 2015):

$$z(y) = \frac{h}{2} \left[ 1 + \tanh\left(\frac{y}{\varepsilon}\right) \right] \tag{1}$$

where  $\varepsilon$  is a fitting parameter. Fitting z (y) to the MD data for the long dislocation lines (30 nm and above) in Fig. 2c yields  $\varepsilon=3.12$  nm for Fe and  $\varepsilon=0.73$  nm for W. An insertion of the fitted values into Eq. (1) can be used to extract the equilibrium kink width analytical, e.g.,  $\sim$ 24b for Fe at zero applied stress, which is in a reasonably good agreement with the values of  $\sim$ 19b extracted from an experimental analysis of the dislocation mobility in high-purity Fe below 250K (Caillard, 2010, 2013). The result in Fig. 2 suggests that the present computer model provides a satisfactory description of the kink structure down to the atomic scale. Most importantly, Eq. (1) and the values of  $\varepsilon$  fitted from our MD data will be applicable in kMC (Stukowski et al., 2015), which treats the kinks on dislocation lines as trapezoidal elastic segments. However, it should be always kept in mind that the obtained  $\varepsilon$  is only for kinks on sufficiently long dislocation lines. A re-calibrated version of this parameter is needed if the dislocation line is sufficiently short, because the shape of a kink on short dislocations is significantly deviated from that on long ones. For instance, to investigate the dependence of the kink width on L, we (i) construct a series of atomistic models for Fe and W samples containing kinked dislocations with L being 3 nm, 5 nm, 10 nm, and 30 nm, respectively; (ii) measure the equilibrium kink width, w; (iii) fit the parameter of  $\varepsilon$  in Eq. (1); and (iv) summarize the obtained results as the following Table 1:

## 3. Kink diffusion in Fe and W under zero applied stress at finite temperature

### 3.1. Tracking the motion of a single dislocation kink in Fe and W

Starting from the equilibrated structure, the dynamics of dislocation kinks in Fe and W under zero applied stress at finite temperature is quantified here. As a first step, the motion of each single kink is tracked. Taking the 120 nm-long dislocation line in Fe as an

**Table 1** The equilibrium width of a kink on dislocations with different L and the fitted values of  $\varepsilon$ .

Simulation Cell Size	Kink Width (Fe)	$\varepsilon$ (Fe)	Kink Width (W)	ε (W)
3 nm	1.6 nm	1.56 nm	0.93 nm	0.33 nm
5 nm	3.7 nm	2.65 nm	1.70 nm	0.66 nm
10 nm	5.9 nm	2.67 nm	2.22 nm	0.67 nm
30 nm	5.9 nm	3.12 nm	2.31 nm	0.73 nm

example, the following Fig. 3a and b presents the time sequences of kink diffusion along a dislocation line at T = 50K.

The instantaneous position of Kink-I and Kink-II are tracked as shown in Fig. 3a and b. Apparently, both of them are in stochastic motions. We can measure the kink diffusion coefficients if we can assure that the motions of the two kinks are uncorrelated with each other. To confirm it, the correlation coefficient between the instantaneous displacements of Kink-I and Kink-II is defined and calculated as:

$$|r| = \left| \frac{\sum_{i=1}^{N} (y_i^I - \overline{y^I}) \cdot (y_i^{II} - \overline{y^{II}})}{\sqrt{\sum_{i=1}^{N} (y_i^I - \overline{y^I})^2} \cdot \sqrt{\sum_{i=1}^{N} (y_i^{II} - \overline{y^{II}})^2}} \right|$$
 (2)

where  $y_i^I$  and  $y_i^{II}$  are the displacements of Kink-I and Kink-II at the *i*-th time step;  $\overline{y_i^I}$  and  $\overline{y_i^{II}}$  are the mean positions of two kinks, N is the total number of output frames. Here we use the initial configuration as a reference to monitor the displacement of each kink. The correlation coefficient between Kink-I and Kink-II along dislocations with a variety of different cell sizes (30 nm and above) are calculated and summarized in Table 2. It is seen that, for both Fe and W, the correlation coefficient is significantly less than 0.1. Such a

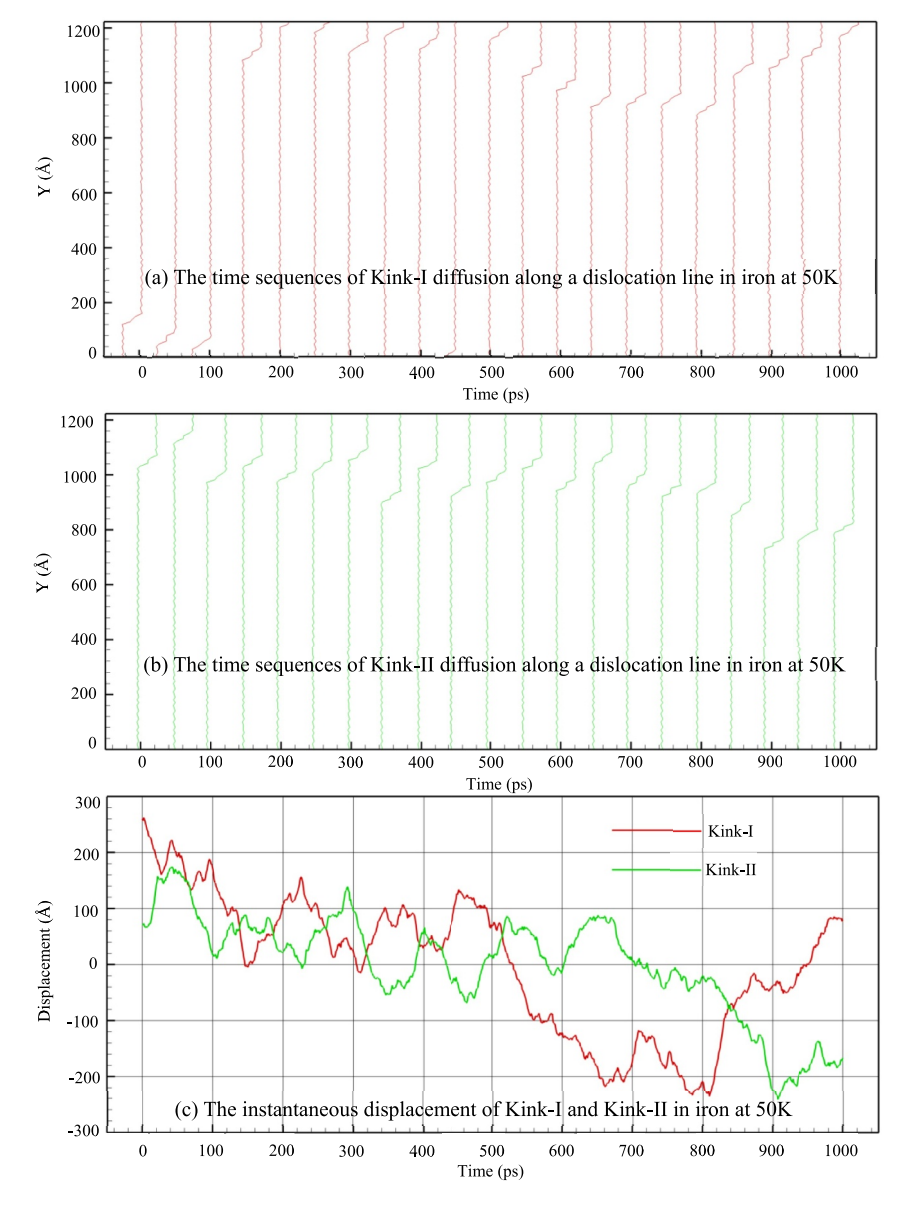


Fig. 3. The time sequences of (a) Kink-I and (b) Kink-II diffusion along a dislocation line with L = 120 nm; and (c) the instantaneous displacements of two kinks, from MD simulations of iron at T = 50K.

small correlation coefficient suggests that the dynamics of Kink-I and Kink-II are uncorrelated with each other when L is at the level of 30 nm and above.

In addition, a correlation coefficient of 0.4 is also obtained in an additional simulation when L is reduced to 15 nm. This result means that, when L is sufficiently short, the motions of Kink-I and Kink-II strongly correlates with each other. To demonstrate such a simulation cell size-dependent correlation between Kink-I and Kink-II, Fig. 4 presents a scatter diagram plot where the instantaneous displacements of the two kinks are used as the data points. It is seen that when L is as short as 15 nm (Fig. 4a), the motions of Kink-I and Kink-II are almost linearly correlated at a later stage, although their motions seem to be independent with each other at the beginning. The negative slope in the linear correlation (Fig. 4a) indicates that the two kinks are moving at constant velocities along opposite directions. The reason for this linear correlation is: the kinks on short dislocation lines can easily move out and re-enter the simulation box due to the PBCs. When this happens, the initially well-separated dislocation dipoles migrate and get closer to each other. As a consequence, the attractive force between the two dislocations in the dipole eventually increases. At a later stage, the kink motions are dominated by a drift induced by such attractive forces and eventually become correlated with each other. Instead, if the dislocation line is sufficiently long (Fig. 4b), the kinks on the two dislocation lines can stochastically migrate a reasonably large distance in a long duration before the two dislocation lines get too close with each other. This, in turn, gives rise to the independent "Brownian-type" diffusive motions of Kink-I and Kink-II (Fig. 4b), which can be safely used for extracting the dynamic properties of kinks, such as diffusion coefficients,  $D_{kink}$  and the dissipation parameter,  $\gamma_{kink}$ .

#### 3.2. Characterizing the kink dynamics and its dependence on the simulation cell size

Starting from the kink trajectories in a duration of tens of picoseconds, we then characterize the kink dynamics through measuring the two key parameters: kink diffusion coefficient ( $D_{kink}$ ) and dissipation parameter ( $\gamma_{kink}$ ). Here,  $\gamma_{kink}$  is referred as a friction which measures the rate of momentum transfer from the diffusing object (a kink in this work) to the heat bath (Coffey and Kalmykov, 2012; Swinburne et al., 2013). It plays an important role in the stochastic motion of dislocation kinks at finite temperature. In this section, the dependence of the kink dynamics on the atomistic simulation cell sizes are systematically investigated.

Firstly, we calculate the mean square displacement (MSD), noted as  $<\Delta y^2>$ , of the kinks over a time duration of t using the following equation:

$$\langle \Delta y^2 \rangle = \sum_{0}^{N-t/\Delta t} \frac{\left(y_{n+t/\Delta t} - y_n\right)^2}{N - t/\Delta t} - \left(\sum_{0}^{N-t/\Delta t} \frac{\left(y_{n+t/\Delta t} - y_n\right)}{N - t/\Delta t}\right)^2 \tag{3}$$

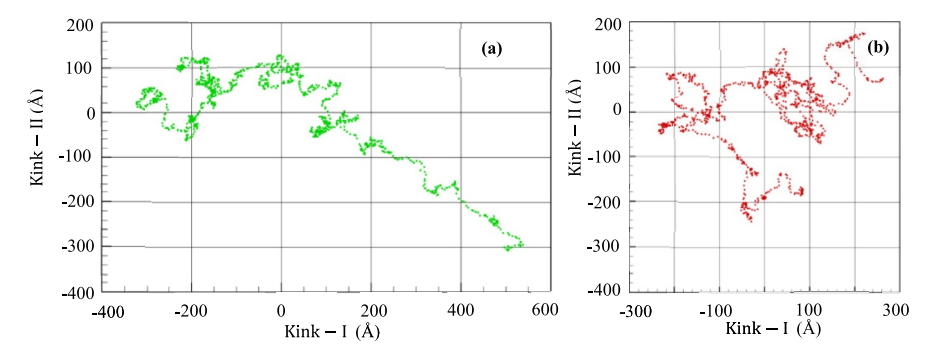
where N is the total number of output frames,  $\Delta t$  is the time increment between the output frames,  $y_n$  is the position of a kink along the y direction at the n-th frame. In each computer model, there are two kinks and thus an averaged MSD curve can be extracted from the stochastic motions of Kink-I and Kink-II. Fig. 5a shows the MSD curves from a series of simulations of kink diffusion along the dislocation lines with seven different lengths in Fe at T = 50K. In parallel, the results from another six sets of simulations of kink diffusion in W using the same computational set-up are also presented in Fig. 5b. It is seen that, within the same time duration, the MSD of kinks in Fe is always one order of magnitude larger than that in W. Therefore, under the same conditions (simulation cell size, temperature, external stresses, etc.), the dislocation kinks always diffuse faster in Fe than they do in W. This finding, together with the different Peierls barrier in Fe and W, may be used to explain why the dislocations in Fe usually move faster than they do in W. This is commonly observed in experiments, especially when the applied stress and temperature are at a relatively low level.

It is recalled that, when a particle (a dislocation kink here) is in a diffusive motion, its MSD will be linearly proportional to the diffusion coefficient through  $< \Delta y^2 > = 2 \times D_{kink} \times t$ . Using the MSD curves in Fig. 5, we measure the kink diffusion coefficient,  $D_{kink}$ , as the slope of each MSD curve. The extracted kink diffusion coefficients,  $D_{kink}$ , are summarized as:

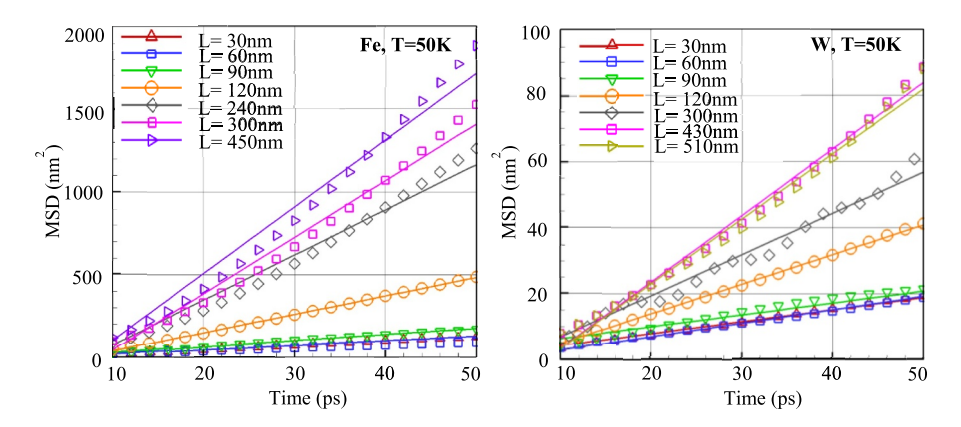
The data in Table .3 and Fig. 5a and b clearly suggests that, for both Fe and W, the kink diffusion coefficients,  $D_{kink}$ , is sensitive to L: the larger L, the higher the slope, and in turn, the larger kink diffusion coefficients. Moreover, for both Fe and W, the  $D_{kink}$  - L correlation can be divided into three characteristic stages: (1) when 30 nm < L < 100 nm,  $D_{kink}$  remains low ( $\sim$ 1.5 nm<sup>2</sup>/ps for Fe and  $\sim$ 0.2 nm<sup>2</sup>/ps for W) and is nearly independent of L; (2) when 100 nm < L < 400 nm,  $D_{kink}$  exhibits a sudden increase and seems to be exponentially proportional to the simulation cell size; (3) when L > 400 nm,  $D_{kink}$  converges to a value ( $\sim$ 21 nm<sup>2</sup>/ps for Fe and  $\sim$ 1.4 nm<sup>2</sup>/ps for W) significantly larger than that in stage-I. Such a three-stage  $D_{kink}$ -L relationship can be correlated with the elastic interaction between the kink and its periodic images, which will be discussed in a later section of this paper. The three-stage  $D_{kink}$ -L relationship, especially the convergence of  $D_{kink}$  when L > 400 nm implies: if a fully converged  $D_{kink}$ , i.e., the kink diffusion coefficients in bulk materials, is desired, the dimension of an atomistic simulation cell along the dislocation line direction needs to be 400 nm and

Table 2 The correlation coefficient between the motions of Kink-I and Kink-II along the two well-separated screw dislocations with a wide range of different simulation cell sizes in Fe and W at T=50K.

Fe	$L=30\; nm$	$L=60\;nm$	$L=90\;nm$	$L=120\;nm$	$L=240\; nm$	$L=300\;nm$	$L=450\;nm$
r	0.012	0.034	0.0086	0.0036	0.00036	0.0003	0.0001
w	$L=30\ nm$	$L=60\;nm$	$L=90\;nm$	$L=120\;nm$	$L=300\; nm$	$L=430\;nm$	$L=510\;nm$
r	0.042	0.060	0.038	0.036	0.014	0.012	0.048



**Fig. 4.** The scatter diagram plots showing the correlation between the instantaneous displacements of Kink-I and Kink-II along (a) 15 nm- and (b) 120 nm-long dislocation lines in W under zero applied stress at T = 50K.



**Fig. 5.** The mean square displacement (MSD) for the kink diffusion along dislocation lines with L ranging from 30 nm to 450 nm in (a) iron; and from 30 nm to 510 nm in (b) tungsten at T = 50K.

even above. Based on this finding, instead of approaching such a large length scale through a direct MD simulation, here we formulate a scaling law to approximate the D<sub>kink</sub>-L dependence. This might be used in higher length scale models for effectively describing the kink diffusion-controlled dislocation mobility in b.c.c. materials in a phenomenological manner.

Here, we propose a form in Eq. (4) to describe the full-scale  $D_{kink}$ -L relationship. It should be noted that Eq. (4) is only a first approximation. If needed, more complex relationships will be formulated under the guidance of more comprehensive atomistic or coarse-grained atomistic simulations (Xiong et al., 2011). The simulation cell size dependence of  $D_{kink}$  is expressed as:

$$D_{kink} = \frac{D_o}{2} + \frac{D_o}{\pi} tan^{-1} \left[ m \left( \frac{L}{L_o} - n \right) \right]$$
 (4)

where  $D_0$  is in the same unit as  $D_{kink}$ , and is the coefficient for kink diffusion along an infinite-long dislocation line;  $L_0$  is an intermediate simulation cell size at which  $D_{kink}$  start to converge to  $D_0$ , and is chosen to be  $L_0 = 200$  nm for both Fe and W; m and n are dimensionless parameters. According to Eq. (4), the critical simulation cell size  $L_c$ , beyond which  $D_{kink}$  starts to sharply increase, can be obtained as  $L_c = mL_0$ . The scaling law in Eq. (4) is then calibrated through fitting it to the data from our atomistic simulations. Fig. 6a and b presents the data (red triangles) from MD together with the fitted scaling laws (green curves) in Fe and W, respectively.

The fitted model parameters are summarized in Table 4. Several main findings are: (i) in Fe and W under zero applied stress at T = 50K,  $D_0$  is  $\sim 2 \times 10^{-5}$  m<sup>2</sup>/s and  $\sim 1.4 \times 10^{-6}$  m<sup>2</sup>/s, respectively. It indicates a one-order-of-magnitude faster kink diffusion in Fe than that in W; (ii) m is found to be 1.0 in Fe and 1.5 in W, respectively. The critical simulation cell sizes are thus calculated as  $L_c = 200$  nm

**Table 3**  $D_{kink}$  for kink diffusion on dislocation lines with different L in Fe and W at T = 50K.

L	30 nm	60 nm	90 nm	120 nm	240 nm	300 nm	450 nm
D <sub>kink</sub> (Fe) (nm <sup>2</sup> /ps)	1.24	1.0	1.8	5.6	13.6	17.1	20.2
L	30 nm	60 nm	90 nm	120 nm	300 nm	430 nm	510 nm
D <sub>kink</sub> (W) (nm <sup>2</sup> /ps)	0.18	0.2	0.18	0.45	0.66	1.0	0.98

for Fe and  $L_c = 300$  nm for W. This corresponds to the turning points from Stage-II in the  $D_{kink}$ -L relationship; (iii) the  $D_{kink}$ -L relation in Fe exhibits a faster convergence to  $D_0$  than that in W. Using the parameterized scaling law in Eq. (4), the kink diffusion coefficient along dislocation lines with an arbitrary  $\boldsymbol{L}$  can be estimated. This can be incorporated into the mobility laws in DD or kMC for describing the kink-controlled dislocation dynamics in b.c.c. materials at a larger length scale than that in MD.

In addition to the simulation cell size, another controlling parameter that affects the kink dynamics in b.c.c. materials is the temperature, T. Following the same procedure above, we measure the temperature-dependent kink diffusion coefficients,  $D_{kink}$ , in Fe and W. Here, in order to heat the system, the velocities of the atoms are gradually rescaled according to a Maxwell-Boltzmann distribution of the given temperature. Once the desired temperature is achieved, the system evolves in a micro-canonical ensemble. The data is then taken when the system temperature is observed to be constant throughout the simulation runs. Fig. 7a and b presents the obtained  $D_{kink}$  -T correlation for the kink diffusion along the dislocation lines with two different lengths in Fe and W, respectively. From Fig. 7a and b, we can clearly see: (i) the kink diffusivities in both Fe and W exhibit a linear temperature dependence; and (ii) the slopes of the linear relationship between the  $D_{kink}$  and T depends on the dislocation length: the longer dislocation line, the larger slope. This result suggests: the kink diffusivities along the long dislocations are more sensitive to temperature than that along the short ones.

The rise of the kink diffusivity with the increase of the temperature in Fig. 7a and b confirms that the kink dynamics here (zero applied stress, finite temperature) are indeed thermally activated. This can be described using Eq. (5) (Swinburne et al., 2013), which contains a main controlling parameter, i.e., the dissipation parameter ( $\gamma_{kink}$ ):

$$D_{kink} = \frac{k_B T}{\gamma_{kink}} \tag{5}$$

where  $k_B$  is the Boltzmann constant.

Through performing a parameter fitting of Eq. (5) to the atomistic data for the relation between the kink diffusion coefficient and the temperature in Fig. 7, we can determine the values of  $\gamma_{kink}$  for kink diffusion along dislocation lines with different lengths in Fe and W. The obtained results are summarized in Table 5. Obviously, in both Fe and W, similar to  $D_{kink}$ ,  $\gamma_{kink}$  exhibits a noticeable simulation cell size dependence: the longer dislocation line, the smaller  $\gamma_{kink}$ .

The obtained  $\gamma_{kink}$  may be then used as inputs for an equation of motion in kMC (Swinburne et al., 2013) to describe the kink dynamics at the continuum level:

$$\gamma_{kink}\dot{y}(t) = \frac{\pi}{a} E_{mig} \sin\left(\frac{2\pi y(t)}{a}\right) + \eta(t) \tag{6}$$

where  $E_{mig}$  is the kink migration barrier, y(t) is the instantaneous position of the kink at time t, a is the lattice constant,  $\eta(t)$  is the Gaussian random variable with an average and standard deviation. That is,

$$\langle \eta(t) \rangle = 0, \quad \langle \eta(t)\eta(t') \rangle = 2 \quad \gamma_{kink}T \quad \delta(t'-t)$$
 (7)

Eq. (6) describes the motion of a dislocation kink undergoing a one-dimensional stochastic motion in a sinusoidal potential. Using the parameters calibrated here in Table 5 as inputs, Eq. (6) may be used to investigate the kink-controlled dislocations in Fe and W at a stress level as low as tens of MPa or even below. This important regime is not directly accessible to atomistic simulations for b.c.c. material which has a high Peierls barrier. Also, the atomistic-informed continuum computer model in Eq. (6) will retain the sensitivity of the kink dynamics to the discrete crystal structure, which is usually not included in conventional dislocation dynamics simulations but is expected to be important for thermally activated dislocation activities. The applications of Eq. (6) to simulating kink dynamics over a wide range of temperatures, stresses, and dislocation geometries fall beyond the scope of this work and will be reported elsewhere.

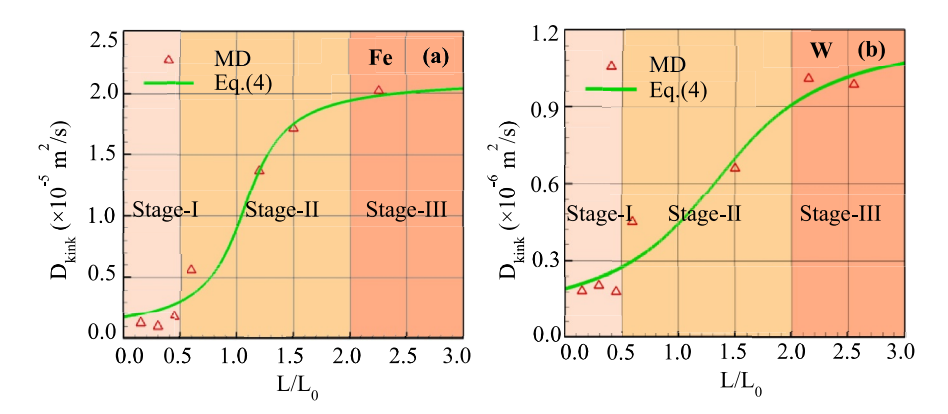


Fig. 6. The L-dependent kink diffusion coefficient in (a) Fe and (b) W.

Table 4

The model parameters of a scaling law for describing the L-dependent kink diffusion.

	$D_o$ ( $\times~10^{-6}~m^2/\text{s})$	п	m
Fe	21.31	1.069	3.664
W	1.234	1.348	1.392

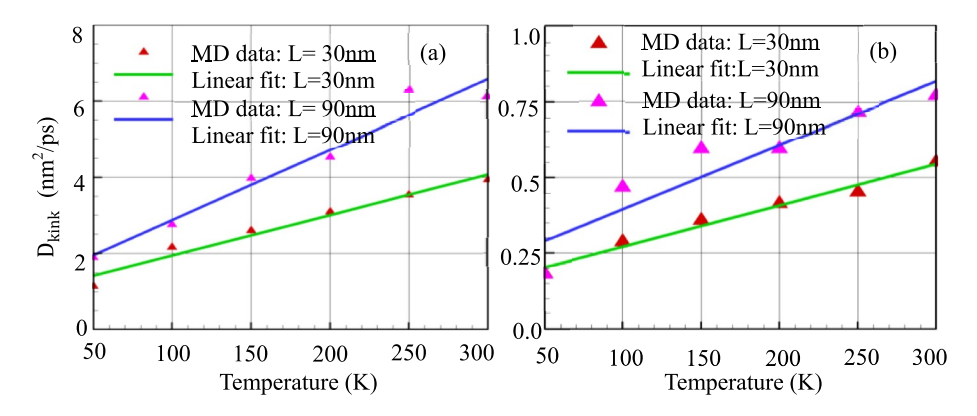


Fig. 7. The temperature dependence of kink diffusivities along dislocation lines in (a) Fe and (b) W.

Table 5  $\gamma_{kink}$  for kink diffusion on dislocation lines with two different lengths in Fe and W. Here the MD data for Kink-I and Kink-II on two dislocation lines are averaged.

	dislocation line ( $L = 30 \text{ nm}$ )	dislocation line (L $= 90 \text{ nm}$ )
Fe	$8.12 \times 10^{-3} \text{ ev} \cdot \text{ps/nm}^2$	$4.66 \times 10^{-3} \text{ ev} \cdot \text{ps/nm}^2$
W	$6.16 \times 10^{-2} \text{ ev} \cdot \text{ps/nm}^2$	$4.10 \times 10^{-2} \text{ ev} \cdot \text{ps/nm}^2$

#### 3.3. Measuring the local stress and relating it to the L-dependent kink dynamics

In addition to the thermal fluctuation, the interaction between a kink and its neighbors is considered to be another main driving force responsible for the stochastic dislocation kink motion. Here, in order to gain insights into the L-dependent kink dynamics, we calculate the kink-induced stress field and relate it to the elastic interaction between kinks.

$$\sigma_{Virial}(\mathbf{x}) = \frac{1}{V} \langle \sum_{k,l} r_{kl} F_{kl} \rangle \tag{8}$$

$$\sigma_{Mechanical}^{\alpha\beta}(\mathbf{x}) = \frac{1}{2} \sum_{k,l} \int_{L_{kl}} F_{kl}^{\alpha} \delta_{A}^{\beta}(\phi - \mathbf{x}) d\phi \ \mathbf{e}^{\alpha} \mathbf{e}^{\beta} \tag{9}$$

In details, we measure the potential part of an atomic-level local stress field,  $\sigma(x)$ , induced by a kink using two distinct formulae: one is the widely used Virial stress formula,  $\sigma_{Virial}(x)$ , in Eq. (8) (Nielsen and Martin, 1985; Hoover, 1986, 1991; Cheung and Yip, 1991) and the other is a recently developed mechanical stress formula,  $\sigma_{Mechanical}(x)$ , in Eq. (9) (Chen, 2016; Chen and Diaz, 2016, 2018; Rigelesaiyin et al., 2018). In Eq. (8), V is the volume of an element cell, such as the Wigner-Seitz cell, around an atom located at the position x;  $r_{kl}$  and  $F_{kl}$  are the distance and the interaction, respectively, between the k-th and the l-th atom; the operator of <> in Eq. (8) means a volume average. By contrast, in Eq. (9), the  $\alpha\beta$ -th component ( $\alpha = 1,2,3$  and  $\beta = 1,2,3$ ) of the local stress at point x is calculated as the average of the  $\alpha$ -th component of the interatomic force,  $F_{kl}$ , over an area,  $\delta_A(\phi \cdot x)$ , whose normal is along the  $\beta$ -th direction. Obviously, as discussed and analyzed in (Chen, 2016; Chen and Diaz, 2016; Rigelesaiyin et al., 2018), the Virial stress formula in Eq. (8) deviates from the concept of the local stress, i.e., the Cauchy stress, in continuum mechanics: Cauchy stress measures the force per unit area whereas the Virial stress calculates the product of interatomic forces and distances, i.e.,  $F_{kl}r_{kl}$ , per unit volume. This distinction suggests that the Virial-type formula may not be appropriate for measuring the local stress, especially the stress field induced by defects (such as dislocations or interfaces) in materials (Rigelesaiyin et al., 2018). By contrast, the mechanical stress formula in Eq. (9) measures the stresses on an atom by averaging the total interatomic force over an element surface. That is, the  $\alpha\beta$ -th component of the stress tensor on an atom is calculated as the  $\alpha$ -th component of the total interatomic force averaged over the area with its normal along the  $\beta$ -th direction. In the previous work by Chen (2016), the mechanical stress formula has been proved to recover the continuum definition of Cauchy stress at the atomic scale. This provides us with confidence to use it for quantifying the dislocation kink-induced local stresses, especially when connecting it with the solution from the theory of elasticity becomes an aim.

When Eq. (8) and Eq. (9) are used for calculating the local stress near a dislocation kink, an atomic row nearby the kinked dislocation line is chosen. And then the stress associated with each atom in this row is measured. Meanwhile, the stress on each atom along the same row in a simulation cell embedded with a dislocation line containing no kinks is also computed. The difference between these two measurements is taken as the stress field induced by a kink. Fig. 8a and Fig. 8b present the kink-induced shear stress ( $\sigma_{yz}$ ) distribution along the dislocation line direction in Fe and W, respectively. The results from the calculations using both Virial and mechanical stress formulas are compared. It is seen that, in both W and Fe, independent of the chosen stress formula, the local stress field at the core of a kink exhibits a singularity and decays away from the kink core. This can be easily understood because the kink core is similar to one dislocation segment with an edge character. Based on the results in Fig. 8, we propose that the stress field induced by a kink can be related with the distance r, away from its core through:

$$\sigma_{xy} \sim \frac{\sigma_0}{r^d}$$
 (10)

where  $\sigma_0$  is the stress at the kink core and n is a model parameter describing how fast the stress decays away from the core. By fitting Eq. (10) to the MD data in Fig. 8, the values of n are found to be 2.19 and 2.17 for Fe and W, respectively, if the Virial stress formula is used. Using Eq. (10), the shear stress acting on a kink by its neighbor which is 120 nm away can be estimated to be 0.06 MPa and 0.16 MPa in Fe and W, respectively. It was reported (Stukowski et al., 2015) that a kink moves at a constant velocity of 8 m/s under a stress of 2 MPa. Thus, a local stress at the level of 0.16 MPa cannot be simply negligible, especially in the absence of any external loading. In contrast, when the mechanical stress formula is used, the values of n in Eq. (10) are 1.75 and 2.30 for Fe and W, respectively. Comparing with what has been obtained using the Virial formula, this result indicates an even slower stress decay away from the kink core. Based on the above local stress analysis, we believe: (i) an accurate measurement of the long-range elastic interaction between a dislocation kink and its periodic images in the atomistic models requires the deployment of a mechanical stress formula; and (ii) this long-range interaction contributes significantly to the L-dependent kink dynamics.

In order to confirm this, first of all, we recall the elasticity solution for the interaction between a kink and its neighbors. In elasticity, under a sufficiently large kink separation (larger than the kink width), the interaction between a kink and its neighbor spans a long range and is considered to be of Coulomb-type (Eshelby, 1962). In details, the elastic energy induced by the kink-kink interaction can be expressed as:

$$E(r) = -\frac{K}{r} \tag{11}$$

where r is the separation between kinks, K is proportional to the material's shear modulus and is equal to  $\mu b^2 h^2 (1 + \nu)/[8\pi (1 - \nu)]$ ,  $\mu$  is the shear modulus, b is the Burgers vector, h is the kink height, and  $\nu$  is the Poisson's ratio. A variety of different forms for K have been proposed (Eshelby, 1962) to account for the finite width or different kink shapes but does not qualitatively change the results to be discussed as below. Therefore, for simplicity, here we choose  $K = \mu b^2 h^2 (1 + \nu)/[8\pi (1 - \nu)]$ . Using Eq. (11), we can calculate the force induced by the interaction between the two separated kinks as:

$$F(r) = -\frac{\partial E}{\partial r} = \frac{K}{r^2} = \frac{\mu b^2 h^2 (1+\nu)}{8\pi (1-\nu)} \frac{1}{r^2}$$
 (12)

Alternatively, if the stress field distribution  $\sigma(r)$  between the two kinks separated by a distance of r is available, the force between them can be calculated by:

$$F(r) = \sigma(r)b \ h \tag{13}$$

Starting from Eq. (13), we can covert the obtained atomistic local stresses to the force, F(r), through multiplying the MD data in

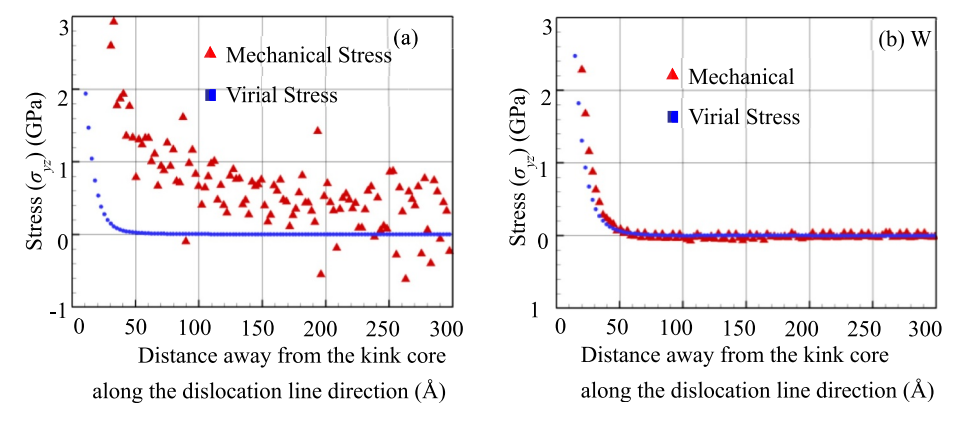


Fig. 8. Kink-induced shear stress away from a kink core along the dislocation in (a) Fe and (b) W.

Fig. 8 by a factor of bh. The obtained results are plotted and compared (Fig. 9a and b) with that from Eq. (12). Several major findings from Fig. 9a and b are: (a) the elastic force between kinks is underestimated when the Virial stress formula is used. This is consistent with our previous results (Rigelesaiyin et al., 2018), in which the Virial stress formula was found to underestimate the stress nearby the material defects; (b) the kink-kink interaction measured from the mechanical stress calculation matches well with the elasticity solution; (c) the force acting on a kink induced by its neighbor 30 nm away is still at the level of  $7 \times 10^{-14}$ N. A force at this level may significantly alternate the kink dynamics given that the effective mass of a single kink per unit length can be estimated as  $8 \times 10^{-16}$  kg/m when considering it as an edge dislocation segment. The limited dimension of the simulation cell along the dislocation line direction leads to a finite separation between a kink and its periodic image, and in turn, a non-negligible force. This force is repulsive in nature because each kink and its periodic image carry the same kink vector. Such a repulsive force causes the significantly slower kink diffusion along a shorter dislocation line (30 nm in length) than that along the longer dislocations (120 nm or above). This explains the cell size dependent kink dynamics in the present atomistic simulations.

#### 4. Summary and discussion

In this work, taking b.c.c. iron and tungsten as the model systems, a series of atomic-level MD simulations are carried out to quantify the dynamics of kink diffusion along a screw dislocation line in high-Peierls-barrier b.c.c. materials. Several major findings are:

- (1) The width of a kink converges when atomistic simulation cell size, L, along the dislocation line direction is sufficiently large. However, when the L is at the nanoscale, for example,  $\sim$ 6 nm in Fe and  $\sim$ 3 nm in W, the equilibrium kink width and kink shape are sensitive to L: the smaller L, the narrower kink width, and the sharper kink core. This is believed to be caused by the repulsive force between a kink and its periodic images in the atomistic computer models;
- (2) In b.c.c. metals exposed to a finite temperature, when a kink is on a sufficiently long dislocation line (*L* = 30 nm or above) and is well separated (40 nm or above) from the other dislocations, its dynamics can be in a Brownian-type diffusion. Otherwise the motion of a kink will be strongly correlated with each other due to the elastic interaction between them;
- (3) The atomistic-calculation-based kink diffusion coefficients,  $D_{kink}$ , for both Fe and W are comparable with that from experiments (Gilbert et al., 2011) and other existing calculations (Swinburne et al., 2013). More importantly,  $D_{kink}$  in Fe is found to be one order of magnitude larger than that in W. Besides the lower Peierls barrier in Fe than that in W, this result provides additional explanation on why the dislocations in Fe move faster than they do in W when these two materials are deformed under a low level of stresses at finite temperature;
- (4) The present atomistic simulations predict a three-stage L-dependent kink dynamics: (a) when L is smaller than a critical value (80 nm in Fe and 100 nm in W),  $D_{kink}$  is nearly insensitive to the change of L; (b) when a kink diffuses along dislocation lines with L being larger than those critical values,  $D_{kink}$  exponentially increases with the increase of L; and (c) when L is 300 nm in Fe and 400 nm or above in W,  $D_{kink}$  nearly converges to the bulk value;
- (5) A scaling law for correlating the  $D_{kink}$  with L is formulated and calibrated using the data from the present atomistic simulations. Such a scaling law can be incorporated into higher order computer models, such as DD or kMC, for understanding the kink-controlled dislocation dynamics in b.c.c. metallic materials at the mesoscopic level;
- (6) In addition to  $D_{kink}$ , the other key parameter of kink dynamics, the friction parameter  $\gamma_{kink}$ , is also quantified through a series of atomistic simulations. Similar to the L-dependent  $D_{kink}$ ,  $\gamma_{kink}$  is found to be also sensitive to the simulation cell size along the dislocation line direction;
- (7) The atomic-level stress analysis demonstrates that the L-dependent kink dynamics originate from the long-range stress field induced by a kink core, which is seen to approximately decay as the second order of the distance away from the kink. This is also consistent with the solution from the theory of elasticity, in which a Coulomb-type long-range elastic interaction between a kink and its neighbors nearby is assumed.

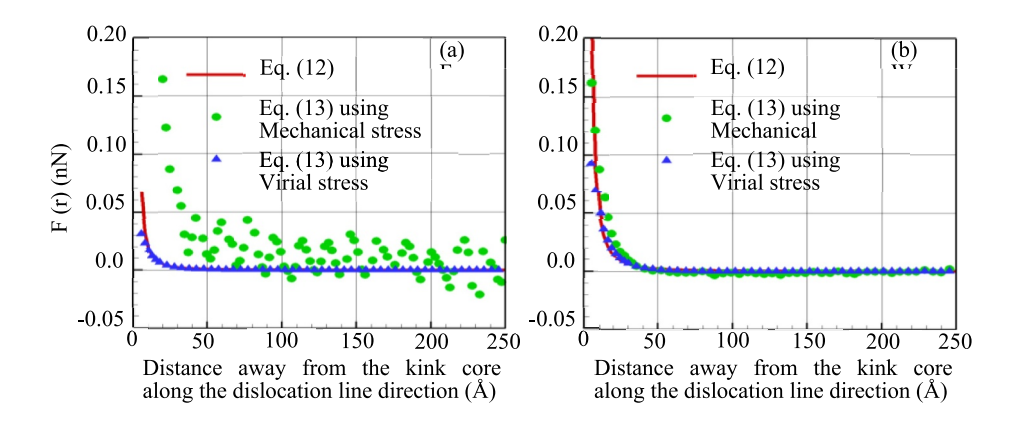


Fig. 9. The force induced by the interaction between a kink and its neighbor in (a) Fe and (b) W.

The above findings may be utilized to advance our understanding of dislocation dynamics in b.c.c. materials by providing a support on (a) interpreting the experimental observations, in which the dislocation mobility in b.c.c. materials was found to be proportional to a dislocation line length (Caillard, 2010, 2013); and (b) formulating a set of kink-controlled mobility laws that can be used in higher length scale computer models such as DD (Van der Giessen and Needleman, 1995, Zbib et al., 2000; Ghoniem et al., 2000; Bulatov et al., 2006; El-Awady, 2015; Po et al., 2016), or kMC (Lin and Chrzan, 1999; Cai et al., 2001; Swinburne et al., 2013) for describing dislocation dynamics in b.c.c. materials at the meso- or even macroscopic level. However, given the limited length scales of the present atomistic computer model, we would like to emphasize: (i) a mapping of the mechanisms revealed from such nanoscale MD simulations to the micro-experimental observation (Caillard, 2010, 2013) is possible but is considered to be only qualitative at this stage. There exists an obvious length scale mismatch between MD and experiments. In particular, it remains very challenging, if not impossible, to accurately quantify the coefficient of a thermal-induced kink diffusion along a dislocation in MD models if a periodic boundary condition is used, because the long-range interaction between a kink and its periodic images will pollute the results. In details, the longest dislocation line in the present MD is ~400 nm in length while the lengths of dislocation lines in experiments (Caillard, 2010, 2013) are microns and above; (ii) an incorporation of the atomistic-simulation-based kink dynamics into the mobility law for kMC and DD is not trivial because the atomistic nature of the kink dynamics has been smeared out during such a "message-passing" procedure. The form of a mobility law and the corresponding model parameters need to be carefully chosen and systematically calibrated to retain the fundamental physics as much as possible. Otherwise, the results from kMC or DD could be misleading. Therefore, as pointed out in (Richman and LeSar, 2006, Kooiman et al., 2015; Beyerlein et al., 2019; McDowell, 2019), in order to bridge the length scale gap between MD, experiments, and mesoscopic-level computer models, a coarse-grained (CG) approach is needed for simultaneously resolving the motion of a µm-long dislocation line and the atomic-level kink diffusion along the line itself (Fig. 10a).

Here we argue that our CG atomistic model (Xiong and Chen, 2009, Deng et al., 2010, Chen et al., 2011, Xiong et al., 2011, 2014, 2016, Xiong and Chen, 2012, Xiong et al., 2012a-b, Xu et al., 2016, 2017b) can be one suitable, if not the best, method to meet this need. Fundamental to the CG method is an atomistic field formulation (Chen, 2006, 2009, 2016; Chen and Diaz, 2016, 2018) that unifies the atomistic and continuum description of materials through an Irving-Kirkwood procedure (Kirkwood, 1946, 1947; Irving and Kirkwood, 1950) in statistical mechanics. This formulation considers the crystalline material as a collection of continuously-distributed lattice cells, within each of which a group of atoms is embedded. The atomic displacement field is then expressed as the sum of a continuum-level lattice deformation and a discrete sub-lattice internal deformation. This two-level description leads to governing equations that are identical in form to the balance equations in continuum theories, which can be used to solve for not only the lattice cell deformation at a continuum level but also the internal motion of atoms at the sub-lattice level. The continuum modeling techniques, such as finite element (FE), can be used to solve these equations. The utilization of FE in regions where materials deform cooperatively leads to the CG model (Xiong et al., 2011, 2012a-b), in which the atomic displacement is constrained using FE shape functions to reduce the number of degree-of-freedom. For modeling material plasticity, an element that conforms to the geometry of a material's primitive cell was adopted, e.g., a rhombohedral element for f.c. c crystals (Xiong et al., 2011). This element ensures that, following nucleation, dislocations can migrate along the element boundaries, which are aligned with the slip planes. Thus, one unique feature of CG is its capability of explicitly accommodating the dislocation activities in a continuum domain without smearing out its atomistic nature. At a fraction of the cost of MD, CG was demonstrated to be applicable for quantifying the dynamics of a submicron-long dislocations (Xiong et al., 2012b; Chen et al., 2018) in f.c.c. materials and their interactions with long-wavelength phonons (Xiong et al., 2014, Chen et al., 2017) or material defects like voids (Xiong et al., 2015) and grain boundaries (Xu et al., 2016). The above results provide us with confidence on using the CG model to describe the complex interplay between the migration of a µm-long dislocation line and the atomic-level kink diffusion along the line as sketched in Fig. 10b. As a first step, we are currently expanding this CG model to quantify the dislocation kink dynamics in b.c.c. materials exposed to a finite temperature. The demonstration of the newly developed finite temperature CG for understanding the kink-controlled dislocation activities in b.c.c. metallic materials and many other high-Peierls-barrier materials will be reported in our future work.

In addition to the length scale limitation, another well-known intrinsic bottleneck of MD is its limited simulation duration at a level of nanoseconds or below. This has constrained its applicability in modeling the rare events such as nucleation, diffusion, and growth in solid materials, which usually occur over a time scale of seconds, days, and even years. Fortunately, as far as the dislocation kinks are concerned, once activated, their migrations are not rare and are within the reach of MD or CG simulations because; (1) the dislocation kink migration barrier in typical b.c.c. metals is found to be extremely low at a level of ~150 meV (Swinburne et al., 2013). Such a low migration barrier implies that the migration of dislocation kinks can be easily activated by a thermal-induced fluctuation at the atomic scale; and (ii) once the dislocation kinks start to move, their migration velocity in b.c.c. metals is at a level of ~100 nm/ns (Stukowski et al., 2015). Such a fast kink migration makes MD or CG an adequate tool for being used to extract a reliable kink diffusion coefficient in a duration of nanoseconds. This can be evidenced by the converged MSD curves that we have presented in Fig. 5. Despite of that, we are fully aware and should emphasize that, distinct from kink migration, a thermal-induced kink nucleation itself is indeed very rare and can be captured by neither MD nor CG due to their limited time scale at this stage. This is also the reason why we did not simulate the kink nucleation process in this work. Instead, we build the dislocation kinks into the model from the very beginning. Nevertheless, a fully atomistic or CG simulation of thermal-activated kink nucleation is considered to be still possible if those methods can be properly integrated with certain multiple timescale theories, techniques, or algorithms, such as transient state theory (Nguyen et al., 2011; Fan et al., 2013), accelerated molecular dynamics (Voter, 1997; Voter et al., 2002), and among many others. This falls beyond the scope of the present work. A practice along this direction is worthy an intensive attempt in the next.

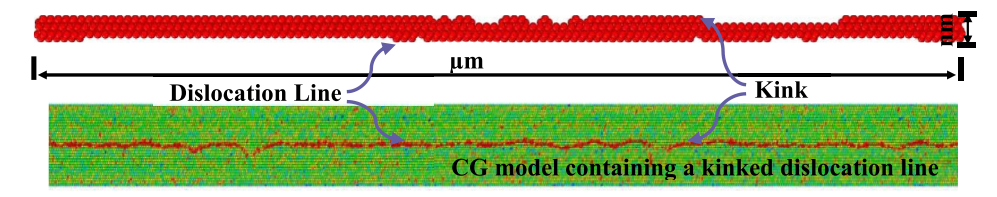


Fig. 10. Multiscale nature of the kink diffusion along dislocations: (a) the atomic level kinks on a µm-long dislocation line; (b) the sketch of a CG model containing a long dislocation line with many kinks.

#### Declaration of competing interest

The authors declare that they have no known competing financial interests or personal relationships that could have appeared to influence the work reported in this paper.

#### CRediT authorship contribution statement

Rigelesaiyin Ji: Formal analysis, Writing - original draft, Data curation. Thanh Phan: Writing - review & editing, Visualization. Hao Chen: Software. Liming Xiong: Supervision, Conceptualization, Methodology, Formal analysis, Writing - review & editing.

#### Acknowledgement

We greatly appreciate the support from NSF (DMR-1807545 and CMMI-1824840). The atomistic simulations in this work are mainly performed on Comet in the Extreme Science and Engineering Discovery Environment through the project of XSEDE-TG-MSS170003.

#### References

Amodeo, J., Dancette, S., Delannay, L., 2016. Atomistically-informed crystal plasticity in MgO polycrystals under pressure. Int. J. Plast. 82, 177-191. Anderson, P.M., Hirth, J.P., Lothe, J., 2017. Theory of Dislocations, third ed. Cambridge University Press. Beyerlein, I., Xu, S., Llorca, J., El-Awady, J.A., Mianroodi, J.R., Svendsen, B., 2019. Alloy design for mechanical properties: conquering the length scales. MRS Bull. 44 (4), 257-265. Brailsford, A.D., 1965. Abrupt kink model of dislocation motion. III. The effect of internal stresses. Phys. Rev. 137 (5A), A1562. Bulatov, V.V., Justo, J.F., Cai, W., Yip, S., 1997. Kink asymmetry and multiplicity in dislocation cores. Phys. Rev. Lett. 79 (25), 5042-5045. Bulatov, V.V., Hsiung, L.L., Tang, M., Arsenlis, A., Bartelt, M.C., Cai, W., Pierce, T.G., 2006. Dislocation multi-junctions and strain hardening. Nature 440 (7088), Cai, W., Bulatov, V.V., Yip, S., Argon, A.S., 2001. Kinetic Monte Carlo modeling of dislocation motion in BCC metals. Mater. Sci. Eng. A 309, 270-273. Cai, W., Bulatov, V.V., 2004, Mobility laws in dislocation dynamics simulations, Mater. Sci. Eng. A 387, 277-281. Caillard, D., 2010. Kinetics of dislocations in pure Fe. Part II. In situ straining experiments at low temperature. Acta Mater. 58 (9), 3504-3515. Caillard, D., 2013. A TEM in situ study of alloying effects in iron. I-solid solution softening caused by low concentrations of Ni, Si and Cr. Acta Mater. 61 (8), 2793-2807 Cereceda, D., Stukowski, A., Gilbert, M.R., Queyreau, S., Ventelon, L., Marinica, M.C., Marian, J., 2013. Assessment of interatomic potentials for atomistic analysis of static and dynamic properties of screw dislocations in W. J. Phys. Condens. Matter 25 (8), 085702.

Chaussidon, J., Fivel, M., Rodney, D., 2006. The glide of screw dislocations in bcc Fe: atomistic static and dynamic simulations. Acta aterialia 54 (13), 3407–3416.

Chen, H., Xu, S., Li, W., Ji, R., Phan, T., Xiong, L., 2018. A spatial decomposition parallel algorithm for a concurrent atomistic-continuum simulator and its preliminary applications. Comput. Mater. Sci. 144, 1-10.

Chen, X., Xiong, L., McDowell, D.L., Chen, Y., 2017. Effects of phonons on mobility of dislocations and dislocation arrays. Scripta Mater. 137, 22-26.

Chen, Y., 2006. Local stress and heat flux in atomistic systems involving three-body forces. J. Chem. Phys. 124 (5), 054113.

Chen, Y., 2009. Reformulation of microscopic balance equations for multiscale materials modeling. J. Chem. Phys. 130 (13), 134706.

Chen, Y., 2016. The origin of the distinction between microscopic formulas for stress and Cauchy stress. EPL (Europhysics Letters) 116 (3), 34003.

Chen, Y., Diaz, A., 2016. Local momentum and heat fluxes in transient transport processes and inhomogeneous systems. Phys. Rev. 94 (5), 053309.

Chen, Y., Diaz, A., 2018. Physical foundation and consistent formulation of atomic-level fluxes in transport processes. Phys. Rev. 98 (5), 052113. Chen, Y., Zimmerman, J., Krivtsov, A., McDowell, D.L., 2011. Assessment of atomistic coarse-graining methods. Int. J. Eng. Sci. 49 (12), 1337–1349.

Cheung, K.S., Yip, S., 1991. Atomic-level stress in an inhomogeneous system. J. Appl. Phys. 70 (10), 5688-5690.

Coffey, W., Kalmykov, Y.P., 2012. The Langevin Equation: with Applications to Stochastic Problems in Physics, Chemistry and Electrical Engineering, vol. 27. World

Scientific. Deng, Q., Xiong, L., Chen, Y., 2010. Coarse-graining atomistic dynamics of brittle fracture by finite element method. Int. J. Plast. 26 (9), 1402-1414.

Dezerald, L., Proville, L., Ventelon, L., Willaime, F., Rodney, D., 2015. First-principles prediction of kink-pair activation enthalpy on screw dislocations in bcc transition metals: V, Nb, Ta, Mo, W, and Fe. Phys. Rev. B 91 (9), 094105.

Domain, C., Monnet, G., 2005. Simulation of screw dislocation motion in iron by molecular dynamics simulations. Phys. Rev. Lett. 95 (21), 215506.

Duesbery, M.S., 1983. On kinked screw dislocations in the bcc lattice—II. Kink energies and double kinks. Acta Metall. 31 (10), 1759-1770.

El-Atwani, O., Hinks, J.A., Greaves, G., Gonderman, S., Qiu, T., Efe, M., Allain, J.P., 2014. In-situ TEM observation of the response of ultrafine-and nanocrystallinegrained tungsten to extreme irradiation environments. Sci. Rep. 4, 4716.

El-Awady, J.A., 2015. Unravelling the physics of size-dependent dislocation-mediated plasticity. Nat. Commun. 6, 5926.

Eshelby, J.D., 1962. The interaction of kinks and elastic waves. Proc. Roy. Soc. Lond. Math. Phys. Sci. 266 (1325), 222-246.

Fan, Y., Osetskiy, Y.N., Yip, S., Yildiz, B., 2013. Mapping strain rate dependence of dislocation-defect interactions by atomistic simulations. Proc. Natl. Acad. Sci. 110 (44), 17756-17761.

Frederiksen, S.L., Jacobsen, K.W., 2003. Density functional theory studies of screw dislocation core structures in bcc metals. Phil. Mag. 83 (3), 365-375. Ghoniem, N.A.M., Tong, S.H., Sun, L.Z., 2000. Parametric dislocation dynamics: a thermodynamics-based approach to investigations of mesoscopic plastic deformation. Phys. Rev. B 61 (2), 913.

Gilbert, M.R., Queyreau, S., Marian, J., 2011. Stress and temperature dependence of screw dislocation mobility in α-Fe by molecular dynamics. Phys. Rev. B 84 (17), 174103.

Gordon, P.A., Neeraj, T., Mendelev, M.I., 2011. Screw dislocation mobility in BCC Metals: a refined potential description for α-Fe. Phil. Mag. 91 (30), 3931–3945. Gordon, P.A., Neeraj, T., Li, Y., Li, J., 2010. Screw dislocation mobility in BCC metals: the role of the compact core on double-kink nucleation. Model. Simulat. Mater. Sci. Eng. 18 (8), 085008.

Groh, S., Marin, E.B., Horstemeyer, M.F., Zbib, H.M., 2009. Multiscale modeling of the plasticity in an aluminum single crystal. Int. J. Plast. 25 (8), 1456–1473. Gurrutxaga-Lerma, B., 2016. The role of the mobility law of dislocations in the plastic response of shock loaded pure metals. Model. Simulat. Mater. Sci. Eng. 24 (6), 06506

Hoover, W.G., 1986. Molecular Dynamics. Springer, Berlin.

Hoover, W.G., 1991. Computational Statistical Mechanics. Elsevier.

Huang, M., Li, Z., 2013. The key role of dislocation dissociation in the plastic behaviour of single crystal nickel-based superalloy with low stacking fault energy: three-dimensional discrete dislocation dynamics modelling. J. Mech. Phys. Solid. 61 (12), 2454–2472.

Hussein, A.M., Rao, S.I., Uchic, M.D., Dimiduk, D.M., El-Awady, J.A., 2015. Microstructurally based cross-slip mechanisms and their effects on dislocation microstructure evolution in fcc crystals. Acta Mater. 85, 180–190.

Irving, J.H., Kirkwood, J.G., 1950. The statistical mechanical theory of transport processes. IV. The equations of hydrodynamics. J. Chem. Phys. 18 (6), 817–829. Kim, J.Y., Jang, D., Greer, J.R., 2010. Tensile and compressive behavior of tungsten, molybdenum, tantalum and niobium at the nanoscale. Acta Mater. 58 (7), 2355–2363.

Kirkwood, J.G., 1946. The statistical mechanical theory of transport processes I. General theory. J. Chem. Phys. 14 (3), 180-201.

Kirkwood, J.G., 1947. The statistical mechanical theory of transport processes II. Transport in gases. J. Chem. Phys. 15 (1), 72-76.

Kooiman, M., Hütter, M., Geers, M.G.D., 2015. Effective mobility of dislocations from systematic coarse-graining. J. Stat. Mech. Theor. Exp. 2015 (6), P06005. Koslowski, M., Cuitino, A.M., Ortiz, M., 2002. A phase-field theory of dislocation dynamics, strain hardening and hysteresis in ductile single crystals. J. Mech. Phys. Solid. 50 (12), 2597–2635.

Kuchnicki, S.N., Radovitzky, R.A., Cuitiño, A.M., 2008, An explicit formulation for multiscale modeling of bcc metals. Int. J. Plast. 24 (12), 2173–2191.

Levitas, V.I., Javanbakht, M., 2014. Phase transformations in nanograin materials under high pressure and plastic shear: nanoscale mechanisms. Nanoscale 6 (1), 162–166.

Li, D., Zbib, H., Sun, X., Khaleel, M., 2014. Predicting plastic flow and irradiation hardening of iron single crystal with mechanism-based continuum dislocation dynamics. Int. J. Plast. 52, 3–17.

Li, J., Wang, C.Z., Chang, J.P., Cai, W., Bulatov, V.V., Ho, K.M., Yip, S., 2004. Core energy and Peierls stress of a screw dislocation in bcc molybdenum: a periodic-cell tight-binding study. Phys. Rev. B 70 (10), 104113.

Lim, H., Hale, L.M., Zimmerman, J.A., Battaile, C.C., Weinberger, C.R., 2015. A multi-scale model of dislocation plasticity in α-Fe: incorporating temperature, strain rate and non-Schmid effects. Int. J. Plast. 73, 100–118.

Lin, K., Chrzan, D.C., 1999, Kinetic Monte Carlo simulation of dislocation dynamics, Phys. Rev. B 60 (6), 3799,

Lothe, J., Hirth, J.P., 1959. Dislocation dynamics at low temperatures. Phys. Rev. 115 (3), 543.

Marinica, M.C., Ventelon, L., Gilbert, M.R., Proville, L., Dudarev, S.L., Marian, J., Willaime, F., 2013. Interatomic potentials for modelling radiation defects and dislocations in tungsten. J. Phys. Condens. Matter 25 (39), 395502.

McDowell, D.L., 2019. Multiscale modeling of interfaces, dislocations, and dislocation field plasticity. Mesoscale Models 195–297.

Naamane, S., Monnet, G., Devincre, B., 2010. Low temperature deformation in iron studied with dislocation dynamics simulations. Int. J. Plast. 26 (1), 84–92. Nielsen, O.H., Martin, R.M., 1985. Quantum-mechanical theory of stress and force. Phys. Rev. B 32 (6), 3780.

Nguyen, L.D., Baker, K.L., Warner, D.H., 2011. Atomistic predictions of dislocation nucleation with transition state theory. Phys. Rev. B 84 (2), 024118.

Patra, A., Zhu, T., McDowell, D.L., 2014. Constitutive equations for modeling non-Schmid effects in single crystal bcc-Fe at low and ambient temperatures. Int. J. Plast. 59, 1–14.

Patra, A., McDowell, D.L., 2016. Crystal plasticity investigation of the microstructural factors influencing dislocation channeling in a model irradiated bcc material. Acta Mater. 110, 364–376.

Pi, Z.P., Fang, Q.H., Liu, B., Liu, Y., Wen, P.H., 2017. Effect of a generalized shape Peierls potential and an external stress field on kink mechanism in a continuum model. Int. J. Plast. 90, 267–285.

Plimpton, S., 1995. Fast parallel algorithms for short-range molecular dynamics. J. Comput. Phys. 117 (1), 1–19.

Po, G., Cui, Y., Rivera, D., Cereceda, D., Swinburne, T.D., Marian, J., Ghoniem, N., 2016. A phenomenological dislocation mobility law for bcc metals. Acta Mater. 119, 123–135.

Proville, L., Ventelon, L., Rodney, D., 2013. Prediction of the kink-pair formation enthalpy on screw dislocations in α-iron by a line tension model parametrized on empirical potentials and first-principles calculations. Phys. Rev. B 87 (14), 144106.

Proville, L., Rodney, D., 2018. Modeling the thermally activated mobility of dislocations at the atomic scale. Handbook of Materials Modeling: Methods: Theory and Modeling, pp. 1–20.

Rigelesaiyin, J., Diaz, A., Li, W., Xiong, L., Chen, Y., 2018. Asymmetry of the atomic-level stress tensor in homogeneous and inhomogeneous materials. Proc. R. Soc. A: Math. Phys. Eng. Sci. 474 (2217), 20180155.

Richman, J.M., LeSar, R., 2006. Issues in the coarse-graining of dislocation energetics and dynamics. Scripta Mater. 54 (5), 735–739.

Rodney, D., Proville, L., 2009. Stress-dependent Peierls potential: influence on kink-pair activation. Phys. Rev. B 79 (9), 094108.

Seeger, A., Holzwarth, U., 2006. Slip planes and kink properties of screw dislocations in high-purity niobium. Phil. Mag. 86 (25-26), 3861-3892.

Srivastava, K., Gröger, R., Weygand, D., Gumbsch, P., 2013. Dislocation motion in tungsten: atomistic input to discrete dislocation simulations. Int. J. Plast. 47, 126–142.

Shinzato, S., Wakeda, M., Ogata, S., 2019. An atomistically informed kinetic Monte Carlo model for predicting solid solution strengthening of body-centered cubic alloys. Int. J. Plast. 122, 319–337.

Srivastava, K., El-Awady, J.A., 2017. Deformation of magnesium during c-axis compression at low temperature. Acta Mater. 133, 282–292.

Stukowski, A., 2009. Visualization and analysis of atomistic simulation data with OVITO-the Open Visualization Tool. Model. Simulat. Mater. Sci. Eng. 18 (1), 015012.

Stukowski, A., Cereceda, D., Swinburne, T.D., Marian, J., 2015. Thermally-activated non-Schmid glide of screw dislocations in W using atomistically-informed kinetic Monte Carlo simulations. Int. J. Plast. 65, 108–130.

Swinburne, T.D., Dudarev, S.L., Fitzgerald, S.P., Gilbert, M.R., Sutton, A.P., 2013. Theory and simulation of the diffusion of kinks on dislocations in bcc metals. Phys. Rev. B 87 (6), 064108.

Tallman, A.E., Swiler, L.P., Wang, Y., McDowell, D.L., 2017. Reconciled top-down and bottom-up hierarchical multiscale calibration of bcc Fe crystal plasticity. Int. J. Multiscale Comput. Eng. 15 (6).

Tang, M., Marian, J., 2014. Temperature and high strain rate dependence of tensile deformation behavior in single-crystal iron from dislocation dynamics simulations. Acta Mater. 70, 123–129.

Terentyev, D., Dubinko, V., Bakaev, A., Zayachuk, Y., Van Renterghem, W., Grigorev, P., 2014. Dislocations mediate hydrogen retention in tungsten. Nucl. Fusion 54 (4), 042004.

Van der Giessen, E., Needleman, A., 1995. Discrete dislocation plasticity: a simple planar model. Model. Simulat. Mater. Sci. Eng. 3 (5), 689.

Ventelon, L., Willaime, F., 2007. Core structure and Peierls potential of screw dislocations in  $\alpha$ -Fe from first principles: cluster versus dipole approaches. J. Comput. Aided Mater. Des. 14 (1), 85–94.

 $Ventelon, L., Willaime, F., Leyronnas, P., 2009. Atomistic simulation of single kinks of screw dislocations in $\alpha$-Fe. J. Nucl. Mater. 386, 26–29.$ 

Verschueren, J., Gurrutxaga-Lerma, B., Balint, D.S., Sutton, A.P., Dini, D., 2018. Instabilities of high speed dislocations. Phys. Rev. Lett. 121 (14), 145502.

- Voter, A.F., 1997. Hyperdynamics: accelerated molecular dynamics of infrequent events. Phys. Rev. Lett. 78, 3908-3911.
- Voter, A.F., Montalenti, F., Germann, T.C., 2002. Extending the time scale in atomistic simulation of materials. Annu. Rev. Mater. Res. 32, 321-346.
- Wang, Z.Q., Beyerlein, I.J., 2011. An atomistically-informed dislocation dynamics model for the plastic anisotropy and tension-compression asymmetry of BCC metals. Int. J. Plast. 27 (10), 1471–1484.
- Weinberger, C.R., Tucker, G.J., Foiles, S.M., 2013. Peierls potential of screw dislocations in bcc transition metals: predictions from density functional theory. Phys. Rev. B 87 (5), 054114.
- Weinberger, C.R., Battaile, C.C., Buchheit, T.E., Holm, E.A., 2012. Incorporating atomistic data of lattice friction into BCC crystal plasticity models. Int. J. Plast. 37, 16–30.
- Wen, M., Ngan, A.H.W., 2000. Atomistic simulation of kink-pairs of screw dislocations in body-centred cubic iron. Acta Mater. 48 (17), 4255-4265.
- Xiong, L., Chen, Y., 2009. Coarse-grained simulations of single-crystal silicon. Model. Simulat. Mater. Sci. Eng. 17 (3), 035002.
- Xiong, L., Tucker, G., McDowell, D.L., Chen, Y., 2011. Coarse-grained atomistic simulation of dislocations. J. Mech. Phys. Solid. 59 (2), 160-177.
- Xiong, L., Chen, Y., 2012. Coarse-grained atomistic modeling and simulation of inelastic material behavior. Acta Mech. Solida Sin. 25 (3), 244-261.
- Xiong, L., Deng, Q., Tucker, G.J., McDowell, D.L., Chen, Y., 2012a. Coarse-grained atomistic simulations of dislocations in Al, Ni and Cu crystals. Int. J. Plast. 38, 86–101.
- Xiong, L., McDowell, D.L., Chen, Y., 2012b. Nucleation and growth of dislocation loops in Cu, Al and Si by a concurrent atomistic-continuum method. Scripta Mater. 67 (7–8), 633–636.
- Xiong, L., McDowell, D.L., Chen, Y., 2014. Sub-THz Phonon drag on dislocations by coarse-grained atomistic simulations. Int. J. Plast. 55, 268-278.
- Xiong, L., Xu, S., McDowell, D.L., Chen, Y., 2015. Concurrent atomistic-continuum simulations of dislocation-void interactions in fcc crystals. Int. J. Plast. 65, 33-42.
- Xiong, L., Rigelesaiyin, J., Chen, X., Xu, S., McDowell, D.L., Chen, Y., 2016. Coarse-grained elastodynamics of fast moving dislocations. Acta Mater. 104, 143–155.
- Xu, S., Xiong, L., Chen, Y., McDowell, D.L., 2016. Sequential slip transfer of mixed-character dislocations across Σ3 coherent twin boundary in FCC metals: a concurrent atomistic-continuum study. Npj Comput. Mater. 2, 15016.
- Xu, S., Startt, J.K., Payne, T.G., Deo, C.S., McDowell, D.L., 2017a. Size-dependent plastic deformation of twinned nanopillars in body-centered cubic tungsten. J. Appl. Phys. 121 (17), 175101.
- Xu, S., Xiong, L., Chen, Y., McDowell, D.L., 2017b. Shear stress-and line length-dependent screw dislocation cross-slip in FCC Ni. Acta Mater. 122, 412-419.
- Zbib, H.M., de la Rubia, T.D., Rhee, M., Hirth, J.P., 2000. 3D dislocation dynamics: stress-strain behavior and hardening mechanisms in fcc and bcc metals. J. Nucl. Mater. 276 (1–3), 154–165.